

A mechanical model for guided motion of mammalian cells

Patrick Bitter, Kristof L. Beck, and Peter Lenz*

Department of Physics, Philipps-Universität Marburg and LOEWE Center for Synthetic Microbiology, Marburg, Germany
(Dated: March 23, 2022)

We introduce a generic, purely mechanical model for environment-sensitive motion of mammalian cells that is applicable to chemotaxis, haptotaxis, and durotaxis as modes of motility. It is able to theoretically explain all relevant experimental observations, in particular, the high efficiency of motion, the behavior on inhomogeneous substrates, and the fixation of the lagging pole during motion. Furthermore, our model predicts that efficiency of motion in following a gradient depends on cell geometry (with more elongated cells being more efficient).

PACS numbers: 87.17.Jj, 87.17.Aa

Motility and directed cell motion play an important role in many biological processes ranging from embryonic development [1–3] to tissue invasion by pathogenic microorganisms [1, 2, 4, 5] and cancer progression [5–8].

Often extracellular cues are used to regulate the decision in which direction the cell will move [9–11]. Depending on these cues one distinguishes between: (1) chemotaxis where directed motion is guided by solvent chemical cues [9]; (2) haptotaxis where substrate-bound cues influence the cell-substrate adhesiveness [12]; and (3) durotaxis where mechanical cues such as substrate rigidity influence the directed motion [6].

Physics-based experimental and theoretical approaches to study these phenomena have attracted considerable interest in the last decade. Many studies have been devoted to bacterial chemotaxis [9, 10, 13–17] and to *Dictyostelium discoideum* as model system for amoeboid migration [11, 18–22]. The main challenge is to analyze and theoretically model the interplay between molecular processes and the emerging macroscopic motion. For amoeboid motion this is further complicated as shape changes have to be taken into account [20–22].

In contrast, the mesenchymal migration of mammalian cells has so far not been studied theoretically. Although many details have been characterized experimentally [7, 23, 24] theoretical studies have focused only on the cell shape during migration [25], on continuum descriptions for cell populations [7, 24] or on special short-term aspects of migration like migration speed [26] or effective adhesiveness [23].

In this paper we study the motility of mammalian epithelial-like cells. They are influenced by a variety of chemical and physical signals, in particular by different mechanical forces [27] and can show a very high efficiency in following all kinds of gradients [28]. Mammalian cells predominantly migrate by a crawling motion [29]. It consists of a cycle of five discrete steps carried out within about ten minutes [1, 3, 5, 23, 26, 29–33]: (1) polarization of the cell yielding a defined leading and a defined lagging pole; (2) formation of protrusions (predominantly) at the leading pole and attachment of the lagging pole, see Fig. 1(a); (3) stabilization of these protrusions by adhe-

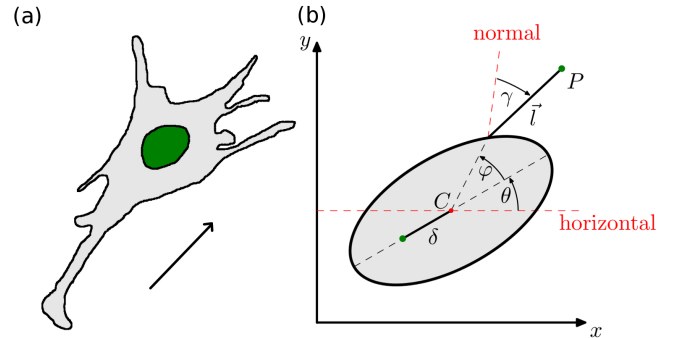


FIG. 1: (a) Typical cell shape as observed in [6] for a cell polarized in the direction of the arrow. The protrusions mainly grow into the forward direction. (b) In our model the polarized cell is represented by an ellipse, the attachments by lines. The position of an attachment point is defined by the length of a protrusion and three angles: the rotation angle of the cell θ , the angle φ for the attachment position on the cell membrane, and the angle γ between the central line and the arm. The distance between the center of the ellipse and the anchor point is δ .

sion to the substrate or the extracellular matrix (ECM); (4) translocation of the cell-body by myosin-mediated contraction; (5) retraction of the rear by loosening the adhesions at the lagging pole. This crawling is propelled by the active lamellipodium at the leading edge which pulls the passive cell body forward [34]. Cell motility depends on the stiffness of the substrate and the ECM. These effects are mediated indirectly via their impact on cell shape [35] and directly through so far unresolved mechanisms referred to as durotaxis [2, 6, 36–38].

The mechanical interaction with the substrate or the ECM can be thought of as a bilinear sequential binding [32], which affects the cell predominantly on the nanoscale through mechanosensing mechanisms [27, 36]. However, cells can also chemically manipulate the ECM, e.g., in case of cancer, where tumor cells stiffen the surrounding ECM [27, 37], and build a rigid stroma around the tumor. This step in ECM stiffness then promotes cells from the outside moving inside, but prevents cells from the inside to migrate outside [39]. In general,

mammalian cells are not passive recipients of mechanical forces, but actively respond by pulling or pushing the ECM [6, 27, 31].

We introduce here a simple, generic model for environment-sensitive motion of fibroblast-like cells. It is solely based on mechanics and is applicable to chemotaxis, haptotaxis, and durotaxis as modes of motility. It provides the first theoretical explanation of the high efficiencies of mesenchymal-like motion independent of cellular morphology. Our model also covers the motility dynamics on large time scales. In particular, we can capture the statistical properties at environmental discontinuities, e.g., a step in substrate stiffness or a step in concentration of a chemo-attractant. These results indicate that regulation of taxis might be based on mechanical forces.

In our model we represent the polarized cell body by an ellipse with major radius R_l and minor radius R_s . The orientation with respect to the x -axis is measured by the angle θ that parameterizes rotation around the center C . To counterbalance the forces of the protrusions the cell is attached to the surface at an anchor point. Moving cells typically have a shape similar to the one shown in fig. 1(a) with a single elongated tail that appears when the cell-body moves forward. This indicates that there is only a single anchor point. The motion occurs in such a way that the cell is effectively rotated around this anchor point, see Fig. 1(b). In principle, cells could also fix the position of the tail with several anchor points. Then, the cell is effectively rotated around these fixed points. For simplicity, we restrict here the analysis to a single anchor point. We assume that the anchor point remains at a fixed position while the cell is not moving. Real cells might change their shape during motion that could lead to a change in the position of the anchor point. However, we do not take such effects into account.

In the following we assume that a molecular mechanism initially polarizes the cell along the x -axis (for example in the presence of a gradient as discussed below). For our purpose we do not explicitly model this process and assume that it leads to a normally distributed initial angle $\theta(t=0)$ with mean $\mu_\theta = 0$. The standard deviation σ_θ was estimated by fitting a normal distribution to the polarization model shown in [40].

The protrusions by which the cells pull themselves forward are represented by adhesive arms that grow out of the ellipse at a random angle φ with probability distributions given by Gaussian distributions centered around $\varphi = 0$ (for the leading pole) and $\varphi = \pi$ (for the lagging pole)

$$p(\varphi) = \frac{p_+}{\sqrt{2\pi}\sigma_+} e^{-\varphi^2/2\sigma_+^2} + \frac{p_-}{\sqrt{2\pi}\sigma_-} e^{-(\varphi-\pi)^2/2\sigma_-^2}. \quad (1)$$

The weights p_+ of the leading pole and $p_- = 1 - p_+ < p_+$ of the lagging pole reflect the initial polarization of the

cell and shift the arm distribution towards the leading pole.

Length and direction of the arms are random. For simplicity, we draw the angle γ between growth direction and surface normal from a Gaussian distribution with mean $\mu_\gamma = 0$ and standard deviation σ_γ . Similarly, the arm length l is distributed normally with mean μ_l and standard deviation σ_l .

Arm formation occurs at constant rate. Every arm applies a linear force on the cell that is proportional to the concentration of a chemoattractant or rigidity of the substrate. Thus, if at time t there are N arms that are attached to the cell body at position $\mathbf{x}_i = \mathbf{x}_i(\varphi_i)$ pointing in direction \mathbf{l}_i (with $1 \leq i \leq N$) the total force on the cell is given by

$$\mathbf{F}(\mathbf{r}_{\text{cell}}, \theta, t) = \sum_{i=1}^N \mathbf{F}_i = \sum_{i=1}^N k(c) \mathbf{l}_i(\mathbf{r}_{\text{cell}}, \theta, \varphi_i), \quad (2)$$

where $k(c) = k_0 c(\mathbf{r}_{\text{arm}})$ depends on the chemoattractant concentration or the substrate rigidity $c(\mathbf{r})$. This results in a translocation of the cell. Furthermore, the arms exert a total torque $M(\mathbf{r}_{\text{cell}}, \theta, t) = \sum_{i=1}^N (\mathbf{x}_i \times \mathbf{F}_i)_z$, that leads to a rotation of the cell that can be interpreted as a gradual repolarization of the cell.

For most of our simulations we used a linear gradient of fixed strength $c_0 = 1/R_l$. This results in a standard deviation of the initial angle of $\sigma_\theta \approx 1$.

To classify the planar cell motion (in the x - y plane), we numerically calculated the moments $\langle x \rangle$, $\langle y \rangle$, $\langle x^2 \rangle$, and $\langle y^2 \rangle$, where $\langle \dots \rangle$ denotes the average over 500 independent runs, see Fig. 2. In these simulations we implemented the above mentioned cycle of independent steps (1)-(5). Starting from the polarized shape [step (1)] we grow N new arms of lengths l_i at angles φ_i in every iteration [steps (2) and (3)]. The new position and orientation of the cell is then obtained by solving $\mathbf{F}(\mathbf{r}_{\text{cell}}, \theta, t) = 0$ and $M(\mathbf{r}_{\text{cell}}, \theta, t) = 0$ independently [step (4)]. Then, all arms are removed [step (5)], the time is increased by δt and the iteration starts over. In the absence of a gradient the cells perform an isotropic random walk. For $N = 10$ (for parameter values see [41]) the effective diffusion coefficients $D_x \approx D_y = 43.77 R_l^2 / \delta t$ were measured by fitting linear functions to $\langle x^2 \rangle$ and $\langle y^2 \rangle$.

In this limit the model can also be solved analytically. From the one-dimensional probability densities of φ , γ and l the two-dimensional probability density of the force induced by an arm can be calculated [41]. We have compared these analytical results with those obtained by direct numerical integration of the model and found excellent agreement. It is interesting to note that this force probability density resembles the shapes of migrating lamellipodial domains of keratocytes [25]. If one assumes that these shape deformations reflect the forces then the forces acting on the cell in our simple probabilistic model are remarkably similar to those exerted by

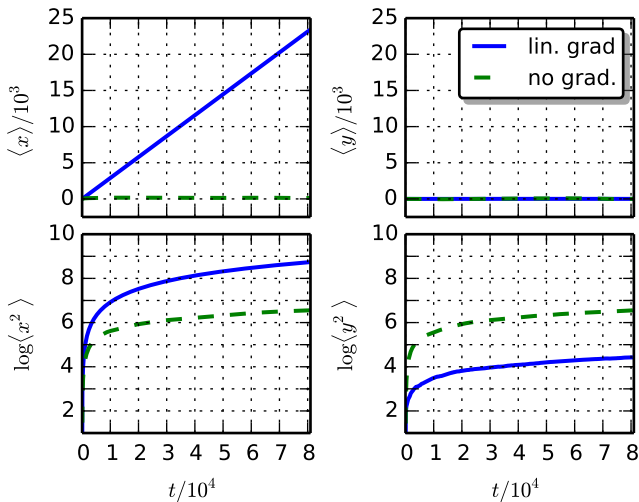


FIG. 2: Classification of cell motion as obtained from the numerically calculated moments $\langle x \rangle$, $\langle y \rangle$, $\langle x^2 \rangle$, and $\langle y^2 \rangle$. In the absence of gradients the cell performs a random walk characterized by vanishing $\langle x \rangle$ and $\langle y \rangle$ and standard deviations that increase with time. In the presence of a gradient this random walk becomes biased. In this case the motion in y -direction is suppressed compared with the case of no gradient. Data were obtained by averaging over 500 independent runs. Length and time are given in units of R_l and δt , respectively.

the actin cytoskeleton of keratocytes.

Next, we consider substrates with gradients. For a linear gradient $c_0 = 1/R_l$ parallel to the x -axis, the cells perform a biased random walk in the gradient direction while the motion in the perpendicular direction is suppressed ~ 135 -fold ($D_y = 0.32R_l^2/\delta t$ in presence of a gradient compared to $D_y = 43.77R_l^2/\delta t$ in absence of a gradient), see Fig. 2. To quantify the efficiency of the motion in following the applied gradient we measured the chemotactic factor

$$CF = \left\langle \frac{L_{\text{grad}}}{L_{\text{tot}}} \right\rangle. \quad (3)$$

Here, L_{tot} is the total path length and L_{grad} the length of the projection in the direction of the gradient.

To investigate the robustness of our model to varying gradients c_0 and its behavior for small gradients we looked at the dependence of CF on c_0 , see Fig. S4 in [41]. For small gradients we see a strong increase in efficiency with the gradient strength, but the efficiency saturates fast to its maximum value of around $CF = 95\%$.

An increase in number of arms results in a speedup of motion and an increase in efficiency, see Fig. 3. However, there is saturation in efficiency and speed for large numbers of arms. If we take into account that 5 to 10 arms with an average length of $7\mu\text{m}$ would roughly cover between 10 and 20% of the surface of the cell (each arm has about $22\mu\text{m}^2$ surface area while the whole cell body has about $1000\mu\text{m}^2$ membrane area [42, 43]) we reach a good

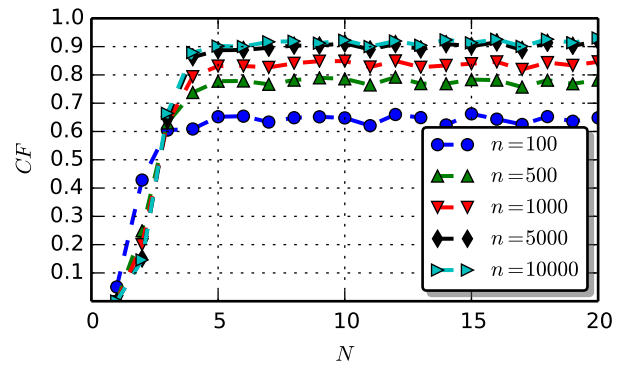


FIG. 3: Efficiency of motion (as quantified by the chemotactic factor CF) as function of the number of arms N for different simulation time steps n .

balance between increase of membrane area and gain of efficiency within this range of N . This number is also comparable to the number of arms found experimentally [6].

Next, we analyzed the influence of the cell geometry on the efficiency of motion. As Fig. 4 shows, CF depends on the geometry of the cell characterized by the ratio R_l/R_s . Thus, more elongated cells (with $R_l > R_s$) have a higher CF . This is somewhat surprising as these cells have a broader force distribution than less elongated cells. However, as we show in [41] CF depends predominantly on the ability of the cell to align with the prescribed gradient. Thus, for more elongated cells this higher ability compensates for the broader force distribution. The CF as determined by the ability to align with the gradient (characterized by a rotational rate α) is given by [41]

$$CF = \exp(x^2) \left[\text{erf} \left(\frac{\pi}{\sqrt{2}\sigma_\theta} - x \right) + \text{erf}(x) \right]. \quad (4)$$

Here, $x = 2^{-1/2}\sigma_\theta\alpha/\chi$ and the opening angle of the force distribution $\chi = \arctan(R_l/R_s \tan \sigma_+)$ parameterizes the dependence on cell geometry.

Lo et. al. [6] have shown that non-moving cells grow longer protrusions on stiff substrates than they do on soft substrates. This implies a regulative effect of the substrate rigidity. To account for this effect in our model we assign each arm i the length

$$l_i + \delta l_i(c) = l_i + \frac{\delta l_{\text{max}}}{1 + \frac{k_c}{c}}, \quad (5)$$

where the regulated elongation $\delta l_i(c)$ depends on the stiffness (or concentration or adhesiveness) $c = c(\mathbf{r}_{\text{arm}})$ at the position of the arm \mathbf{r}_{arm} .

If we increase the average arm length, we see an increase in efficiency that saturates for longer arms, see Fig. S5 in [41]. This rise in efficiency comes with an increase in speed. If we use the concentration-dependent

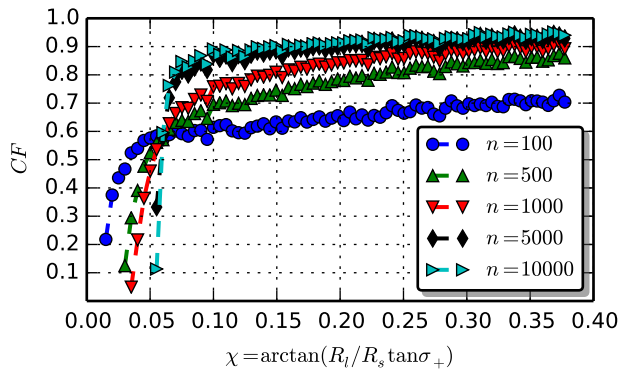


FIG. 4: Chemotactic factor CF is shown as function of cell geometry characterized by R_l/R_s . More elongated cells follow with higher efficiency the gradient (of strength $c_0 = 1/R_l$). The data shown are for different simulation time steps n . For smaller n (i.e. earlier simulation times), CF still depends on the initial alignment of the cells. With increasing n the cells align with the gradient increasing in this way CF . However, as can be seen only cells with $\chi > 0.06$ (i.e. cells which are sufficiently elongated) are able to align with the gradient.

regulation of arm lengths we see a 1% increase in maximum efficiency compared to the unregulated system, but the same efficiency is reached with an average arm length up to 40% shorter compared to the unregulated system.

The above results are robust with respect to variations in the standard deviations of the distributions for φ and γ . CF remains nearly constant for σ_+ and σ_γ in a range from $\sim 0.01\pi$ to 0.2π . For even broader distributions we see a decrease in efficiency as a result of insufficient polarization of the cell. Experimentally, it has been observed that the protrusions grow almost in the normal direction out of the surface of the cells, and that the protrusions are located around a narrow region at the leading pole [5, 44–46]. We find a similar behavior (and the associated high efficiencies in motion) only for distributions with small standard deviations indicating that φ and γ are tightly regulated.

Furthermore, cell motion shows an interesting dependence on the position of the anchor point of the cell to the substrate quantified by the parameter δ . If this point is shifted towards the leading pole, i.e. closer to the protrusions at the front, the torque exerted by these arms is reduced due to the shorter lever arm and the efficiency drops sharply to zero indicating that the cell is not able to follow the gradient at all (see Fig. 5). This indicates that the efficiency in following a gradient is dominated by protrusions close to the leading pole.

Cells often encounter inhomogeneous substrates. As a general scenario, we analyze the movement towards a step in substrate rigidity where crawling cells show an interesting behavior. At these steps (that could represent the transition from a rigid stroma of a tumor to

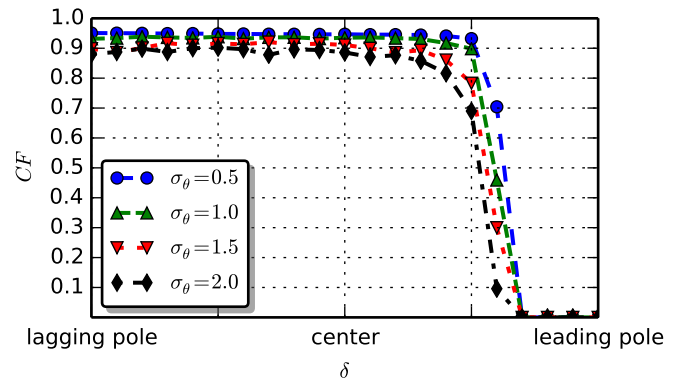


FIG. 5: Dependence of CF on the position of the anchor point to the substrate. The distance of this point from the center of the ellipse is denoted by δ . As this point moves from the center of the ellipse towards the leading pole, CF drops sharply to zero. This indicates that in order to be able to follow a prescribed gradient the cells need to have a defined leading pole and an anchor point sufficiently far away from this pole.

the softer surroundings [27]) cells tend to move from the softer substrate to the stiffer substrate [39]. Cells moving in this direction are only weakly influenced by the step. They keep moving but their trajectory bends towards the direction perpendicular to the step, see Fig. 6. We observed that the relation between the angle of the cell before and after the step obeys a refraction law similar to that of light allowing us to characterize the motion by refraction indices, see Fig. 6(a). The ratio of refraction indices $n_{\text{Soft}}/n_{\text{Stiff}} = \sin \theta_{\text{out}}/\sin \theta_{\text{in}}$ decreases with increasing step size $s = c_1/c_0$, where c_0 and c_1 are the stiffness of the softer and stiffer region, respectively.

On the other hand, a step from a stiff substrate to a softer substrate represents a barrier for cells. The passing probability depends on the step height. From the distribution of the minimal x -positions encountered by the cells during 500 iterations, we can calculate the probability of a cell moving across the step, which we define as transmission coefficient $T_C = \int_{-\infty}^{x_{\text{step}}} p(x) = p(x < x_{\text{step}})$, where $p(x)$ is the probability to find a cell that traveled to position x , and x_{step} is the position of the step, see Fig. 6(b). This coefficient decreases as the step size increases showing that the barrier effect becomes much stronger for larger steps, see Fig. S7 in [41].

Finally, we wanted to compare our results with other types of cellular motion. However, there are neither theoretical nor experimental data available for the efficiency of mammalian cell motion as function of gradient strength. We therefore decided to compare our model with data for swim-tumble chemotaxis, the standard model for cellular motion. More specifically we tested our results against a two-dimensional swim-tumble model for bacterial chemotaxis with a parameter set optimized for

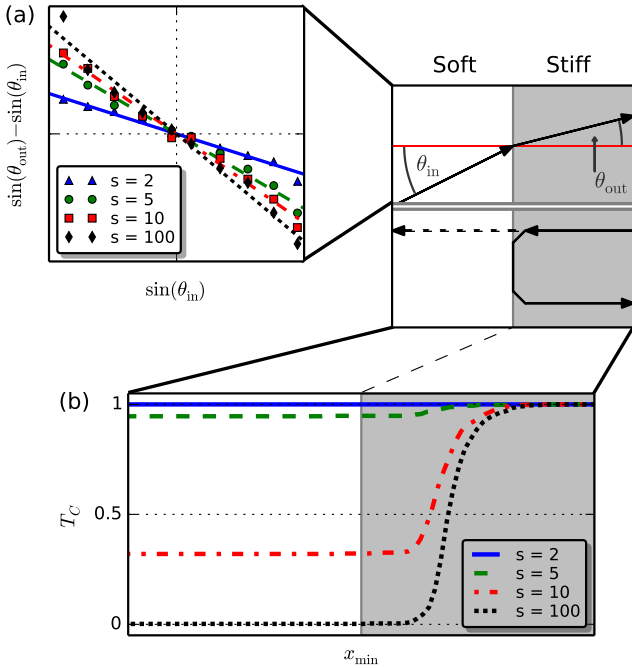


FIG. 6: Transition at a sharp step. (a) If cells move from the soft region to the stiff region one finds a refractive behavior depending on the step size s . (b) Cells moving from the stiff to the soft region experience a barrier that they overcome with a step-size-dependent transmission coefficient. For large step sizes no cells cross the barrier while for small step sizes almost all cells are able to cross it.

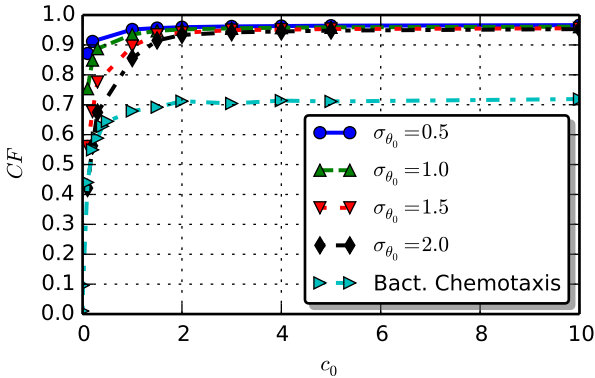


FIG. 7: Variation of the efficiency with the gradient strength c_0 . The cells reach their maximum efficiency at rather small gradients compared to a swim-tumble model of bacterial chemotaxis (based on [9, 10]).

efficiency [9, 10, 41]. As Fig. 7 shows our model yields significantly higher efficiencies than the swim-tumble model.

To summarize, in this study we have introduced a generic mechanical model for environment-sensitive motion of mammalian cells. Motion occurs by polarized growth of protrusions which push and rotate the cell. The description of molecular interactions occurs on a

coarse-grained level effectively entering into the probability distribution for arm growth, see Eq. (1). It is not the goal of this simplified model to achieve a detailed (molecular) description of cellular motility. Rather, we introduce it to analyze the influence of mechanical forces on the regulation of fibroblast motion.

The agreement of our findings with the experimental observations indicates that mechanical forces indeed play a significant role in this process. More specifically, the observed high efficiency in following a gradient is a robust feature of our model (see figs. 4 and 7). We find for a large parameter range chemotactic factors close to 1 as observed experimentally in [28]. Furthermore, the results on the motion in inhomogeneous environments are in good agreement with the experimental observations at steps in substrate rigidity [39].

Our analysis identifies two geometrical factors that have a significant impact on efficiency of cell motion: the position of the anchor point and the geometry of cell quantified by the ratio of major to minor radius. For both quantities we make specific theoretical predictions (figs. 4 and 5) that are experimentally testable.

Furthermore, the moments $\langle x \rangle$, $\langle x^2 \rangle$, $\langle y \rangle$ and $\langle y^2 \rangle$ can be easily measured for individual cells of different geometry for different gradients. By comparing these data with our theoretical predictions (Fig. 7 and Figs. S5 and S6 in [41]) information can be obtained about the concentration dependent regulation of arm lengths. To check our results concerning steps in concentration, adhesiveness and stiffness, one could use the methods presented in [39] to produce flat substrates of different stiffness and measure the polarization axes of the cells before and after the interface as well as the transmission coefficients with time-lapse microscopy.

There are many possible extensions of our model. In future work we will take into account the mechanical effects that the cells have on the substrate. If cells attach protrusions to the substrate and contract, they locally stiffen the substrate. This local stiffening of the substrate might lead to an effective attraction between two cells in proximity, in this way promoting aggregation.

* Electronic address: peter.lenz@physik.uni-marburg.de

- [1] M. Chicurel, *Science* **295**, 606 (2002).
- [2] D. Gray, J. Tien, and C. Chen, *J. Biomed. Mater. Res.* **66**, 605 (2003).
- [3] A. Huttenlocher and A. R. Horwitz, *Cold Spr. Harbor Perspec. Biol.* **3**, a005074 (2011).
- [4] J. Prost, J.-F. Joanny, P. Lenz, and C. Sykes, *The physics of Listeria Propulsion in Cell Motility*, edited by P. Lenz (2008).
- [5] J. T. Parsons, A. R. Horwitz, and M. A. Schwartz, *Nat. Rev. Mol. Cell Biol.* **11**, 633 (2010).
- [6] C. M. Lo, H. B. Wang, M. Dembo, and Y. L. Wang, *Biophys. J.* **79**, 144 (2000).

- [7] A. Gerisch and M. A. J. Chaplain, *J. Theor. Biol.* **250**, 684 (2008).
- [8] F. Bordeleau and L. Galarneau, *Mol. Biol. Cell* **21**, 1698 (2010).
- [9] R. Macnab and D. Koshland, *Proc. Natl Acad. Sci. USA* **69**, 2509 (1972).
- [10] M. J. Tindall, P. K. Maini, S. L. Porter, and J. P. Armitage, *Bull. Math. Biol.* **70**, 1570 (2008).
- [11] H. Levine, and W.-J. Rappel, *Directed Motility and Dictyostelium Aggregation in Cell Motility*, edited by P. Lenz (2008).
- [12] S. B. Carter, *Nature (London)* **208**, 1183 (1965).
- [13] M. J. Tindall, S. L. Porter, P. K. Maini, G. Gaglia, and J. P. Armitage, *Bull. Math. Biol.* **70**, 1525 (2008).
- [14] J. Adler, *Science* **153**, 708 (1966).
- [15] J. Adler, *Annu. Rev. Biochem.* **44**, 341 (1975).
- [16] Y. Tu, T. S. Shimizu, and H. C. Berg, *Proc. Natl Acad. Sci. USA* **105**, 14855 (2008).
- [17] X. Zhu, G. Si, N. Deng, Q. Ouyang, T. Wu, Z. He, L. Jiang, C. Luo, and Y. Tu, *Phys. Rev. Lett.* **108**, 128101 (2012).
- [18] P. Fisher, R. Merkl, and G. Gerisch, *J. Cell Biol.* **108**, 973 (1989).
- [19] D. Fuller, W. Chen, M. Adler, A. Groisman, H. Levine, W.-J. Rappel, and W. F. Loomis, *Proc. Natl Acad. Sci. USA* **107** (2010).
- [20] I. Hecht, M. L. Skoge, P. G. Charest, E. Ben-Jacob, R. A. Firtel, W. F. Loomis, H. Levine, and W.-J. Rappel, *PLoS Comput. Biol.* **7**, e1002044 (2011).
- [21] M. Buenemann, H. Levine, W.-J. Rappel, and L. M. Sander, *Biophys. J.* **99**, 50 (2010).
- [22] B. A. Camley, Y. Zhao, B. Li, H. Levine, and W.-J. Rappel, *Phys. Rev. Lett.* **111**, 158102 (2013).
- [23] M. H. Zaman, R. D. Kamm, P. Matsudaira, and D. A. Lauffenburger, *Biophys. J.* **89**, 1389 (2005).
- [24] A. Häcker, *J. Math. Biol.* **64**, 361 (2012).
- [25] B. Rubinstein, K. Jacobson, and A. Mogilner, *Multiscale Modeling & Simulation* **3**, 413 (2005).
- [26] P. A. DiMilla, K. Barbee, and D. A. Lauffenburger, *Biophys. J.* **60**, 15 (1991).
- [27] D. T. Butcher, T. Alliston, and V. M. Weaver, *Nat. Rev. Cancer* **9**, 108 (2009).
- [28] E. Theveneau, L. Marchant, S. Kuriyama, M. Gull, B. Moepps, M. Parsons, and R. Mayor, *Dev. Cell* **19**, 39 (2010).
- [29] K. Keren and J. A. Theriot, *Biophysical Aspects of Actin-Based Cell Motility in Fish Epithelial Keratocytes in Cell Motility*, edited by P. Lenz (2008).
- [30] A. Mogilner, *J. Math. Biol.* **58**, 105 (2009).
- [31] D. A. Lauffenburger and A. F. Horwitz, *Cell* **84**, 359 (1996).
- [32] A. Pathak and S. Kumar, *PloS one* **6**, e18423 (2011).
- [33] A. J. Ridley, M. A. Schwartz, K. Burridge, R. A. Firtel, M. H. Ginsberg, G. Borisy, J. T. Parsons, and A. R. Horwitz, *Science* **302**, 1704 (2003).
- [34] P. Friedl, *Curr. Opin. Cell Biol.* **16**, 14 (2004).
- [35] W. R. Holmes and L. Edelstein-Keshet, *PLoS Comput. Biol.* **8**, e1002793 (2012).
- [36] L. Trichet, J. Le Digabel, R. J. Hawkins, S. R. K. Vedula, M. Gupta, C. Ribault, P. Hersen, R. Voituriez, and B. Ladoux, *Proc. Natl Acad. Sci. USA* **109**, 6933 (2012).
- [37] P. P. Provenzano, D. R. Inman, K. W. Eliceiri, S. M. Trier, and P. J. Keely, *Biophys. J.* **95**, 5374 (2008).
- [38] T. Yeung, P. C. Georges, L. A. Flanagan, B. Marg, M. Ortiz, M. Funaki, N. Zahir, W. Ming, V. Weaver, and P. A. Janmey, *Cell Motil. Cytoskeleton* **60**, 24 (2005).
- [39] F. Bordeleau, L. N. Tang, and C. A. Reinhart-King, *Phys. Biol.* **10**, 065004 (2013).
- [40] H. Levine and W.-J. Rappel, *Phys. Today* **66**, 24 (2013).
- [41] See Supplemental Material for further information about analytical results and parameter values.
- [42] D. Raucher and M. P. Sheetz, *Biophys. J.* **77**, 1992 (1999).
- [43] L. C. Baxter, V. Frauchiger, M. Textor, I. Gwynn, and R. G. Richards, *Eur. Cell. Mater.* **4**, 1 (2002).
- [44] I. V. Maly and G. G. Borisy, *Proc. Natl Acad. Sci. USA* **98**, 11324 (2001).
- [45] T. M. Svitkina, E. A. Bulanova, O. Y. Chaga, D. M. Vignjevic, S.-I. Kojima, J. M. Vasiliev, and G. G. Borisy, *J. Cell Biol.* **160**, 409 (2003).
- [46] A. Mogilner and B. Rubinstein, *Biophys. J.* **89**, 782 (2005).

Supplemental Material: A mechanical model for guided motion of mammalian cells

ANALYTICAL RESULTS

Force distribution

The cell is represented by an ellipse with semiaxis $R_l \geq R_s$ (see Fig. S1). An adhesive arm grows out of the ellipse at angle φ . We now choose a coordinate system $(x^{\text{sa}}, y^{\text{sa}})$ with the fixed counterpart of the protrusions as origin and the semimajor axis as abscissa. The vector to the origin of an arbitrary arm is given by

$$\mathbf{r}_{\text{arm}} = \begin{pmatrix} R_l (\cos \varphi - \delta) \\ R_s \sin \varphi \end{pmatrix}. \quad (\text{S.1})$$

The angle between the vector to the attachment point and the abscissa is

$$\varphi' = \arctan \left(\frac{R_s \sin(\varphi)}{R_l (\cos \varphi - \delta)} \right). \quad (\text{S.2})$$

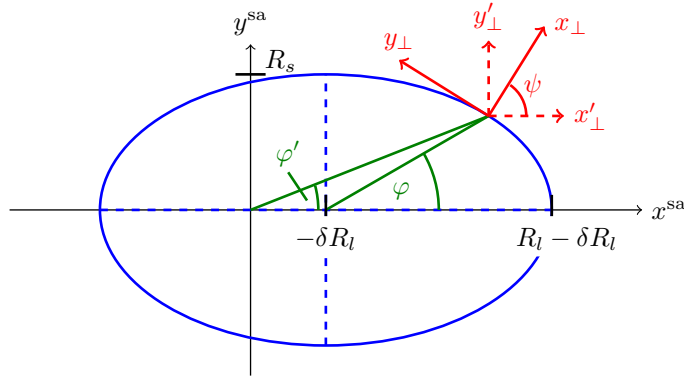


FIG. S1: Ellipse in the coordinate system with fixed counterpart of the protrusions as origin and the semimajor axis as abscissa. Vectors to the attachment point from the origin and from the center of the ellipse are shown in green. The coordinate systems in the attachment point are shown in red: solid lines for the system with one axis perpendicular to the surface, dashed lines for the system rotated parallel to the system of the semiaxis.

Length l and direction γ of the arms are Gaussian distributed

$$p(\gamma) = \frac{1}{\sqrt{2\pi}\sigma_\gamma} \exp \left[-\frac{1}{2} \left(\frac{\gamma}{\sigma_\gamma} \right)^2 \right], \quad p(l) = \frac{1}{\sqrt{2\pi}\sigma_l} \exp \left[-\frac{1}{2} \left(\frac{l - \bar{l}}{\sigma_l} \right)^2 \right]. \quad (\text{S.3})$$

Here, the angle γ is measured relative to the normal of the ellipse in the attachment point. The probability to find an arm with length l and angle γ is

$$p(l, \gamma) = p(l)p(\gamma) = \frac{1}{\sqrt{2\pi}\sigma_\gamma} \exp \left[-\frac{1}{2} \left(\frac{\gamma}{\sigma_\gamma} \right)^2 \right] \frac{1}{\sqrt{2\pi}\sigma_l} \exp \left[-\frac{1}{2} \left(\frac{l - \bar{l}}{\sigma_l} \right)^2 \right]. \quad (\text{S.4})$$

The force caused by an arm with length l and angle γ is given by

$$\mathbf{F}^\perp = kl \begin{pmatrix} \cos \gamma \\ \sin \gamma \end{pmatrix} \equiv \begin{pmatrix} F_x^\perp \\ F_y^\perp \end{pmatrix}, \quad (\text{S.5})$$

in the coordinate system (x_\perp, y_\perp) in the attachment point (see Fig. S1). In the absence of a gradient we can assume $k = 1$.

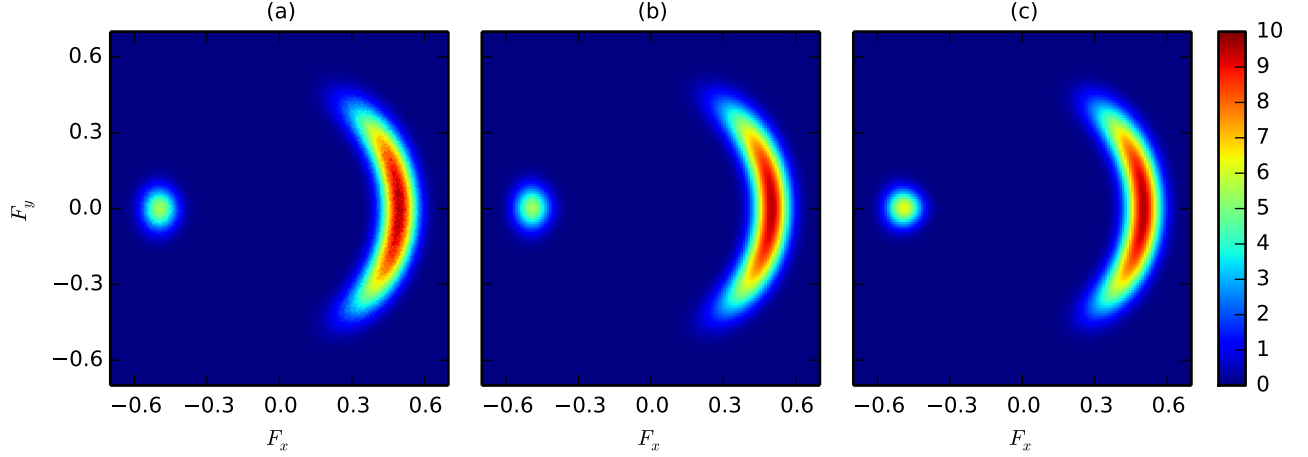


FIG. S2: Probability density for the force (F_x, F_y) . (a) Numerical result; (b) analytical result (S.9) (for same set of parameters); (c) analytical result in the approximation (S.10).

The probability to have a force (F_x^\perp, F_y^\perp) is

$$p^\perp(F_x^\perp, F_y^\perp) = \frac{1}{2\pi\sigma_l\sigma_\gamma} \frac{1}{\sqrt{F_x^{\perp 2} + F_y^{\perp 2}}} \exp\left[-\frac{1}{2}\left(\frac{\sqrt{F_x^{\perp 2} + F_y^{\perp 2}} - \bar{l}}{\sigma_l}\right)^2\right] \exp\left[-\frac{1}{2}\left(\frac{\arctan(F_y^\perp, F_x^\perp)}{\sigma_\gamma}\right)^2\right], \quad (\text{S.6})$$

where we denote by $\arctan(u, v)$ the arc tangent of $\frac{u}{v}$ taking into account the quadrant of the point (u, v) .

To get the force in the coordinate system of the semiaxes, we need to rotate by the angle

$$\psi = \arctan(R_l \sin \varphi, R_s \cos \varphi). \quad (\text{S.7})$$

Thus,

$$\begin{aligned} p_\varphi^{\text{sa}}(F_x, F_y) &= p_\varphi^\perp(F_x^\perp, F_y^\perp) \equiv p^\perp(F_x \cos \psi + F_y \sin \psi, -F_x \sin \psi + F_y \cos \psi) \\ &= \frac{1}{2\pi\sigma_l\sigma_\gamma} \frac{1}{\sqrt{F_x^2 + F_y^2}} \exp\left[-\frac{1}{2}\left(\frac{\sqrt{F_x^2 + F_y^2} - \bar{l}}{\sigma_l}\right)^2\right] \\ &\quad \times \exp\left[-\frac{1}{2}\left(\frac{\arctan(-F_x R_l \sin \varphi + F_y R_s \cos \varphi, F_x R_s \cos \varphi + F_y R_l \sin \varphi)}{\sigma_\gamma}\right)^2\right]. \end{aligned} \quad (\text{S.8})$$

This probability density is valid for any (fixed) φ . The complete density is given by

$$p^{\text{sa}}(F_x, F_y) = \int_{-\pi}^{\pi} d\varphi p_\varphi^{\text{sa}}(F_x, F_y) p(\varphi), \quad (\text{S.9})$$

which has to be calculated numerically. The result shown in Fig. S2 is in good agreement with the numerical data.

As Fig. S2 shows the distributions of γ and φ are rather sharp (i.e. $\sigma_{\varphi-} < \sigma_\gamma \ll 1$). Therefore, we can approximate the corresponding Gaussian functions by delta functions leading to

$$\begin{aligned} p^{\text{sa}}(F_x, F_y) &\approx \frac{p_+}{2\pi\sigma_l\sigma_{\varphi+}} \frac{R_l R_s \sqrt{F_x^2 + F_y^2}}{R_l^2 F_x^2 + R_s^2 F_y^2} \exp\left[-\frac{1}{2}\left(\frac{\sqrt{F_x^2 + F_y^2} - \bar{l}}{\sigma_l}\right)^2\right] \exp\left[-\frac{1}{2}\left(\frac{\arctan(R_s F_y, R_l F_x)}{\sigma_{\varphi+}}\right)^2\right] \\ &\quad + \frac{p_-}{2\pi\sigma_l\sigma_\gamma} \frac{1}{\sqrt{F_x^2 + F_y^2}} \exp\left[-\frac{1}{2}\left(\frac{\sqrt{F_x^2 + F_y^2} - \bar{l}}{\sigma_l}\right)^2\right] \exp\left[-\frac{1}{2}\left(\frac{\arctan(-F_y, -F_x)}{\sigma_\gamma}\right)^2\right]. \end{aligned} \quad (\text{S.10})$$

From this approximation, we conclude that the width of the distribution is given by σ_l in radial direction and by $\sigma_{\varphi+}$ and σ_γ in angular direction. We define χ as the angle, for which $\arctan(R_s F_y, R_l F_x) \leq \sigma_{\varphi+}$, i.e.

$$\chi = \arctan\left(\frac{R_l}{R_s} \tan \sigma_{\varphi+}\right). \quad (\text{S.11})$$

Thus, χ quantifies the ability of the cell to move straight ahead and/or turn towards a given gradient. It depends on $\sigma_{\varphi+}$ and on the geometric factor $\frac{R_l}{R_s}$.

Model for motion along gradients

To investigate the influence of the opening angle on the ability to follow a gradient we analyze a somewhat simplified scenario: we neglect all effects from the back of the cell and do not take into account the torque.

In a first step we describe the motion as a random walk. In doing so we keep track of the position and direction of cell. In each step the cell follows its direction for a constant distance and then changes direction by an angle $\pm\eta$ relative to its current direction. The probabilities for selecting $+\eta$ and $-\eta$ are denoted by p and $1-p$, respectively. The probability that after N steps the cell is rotated n times by η and $N-n$ times by $-\eta$ (resulting in a net rotation of $(2n-N)\eta$) is given by

$$P_N(n) = \binom{N}{n} p^n (1-p)^{N-n}. \quad (\text{S.12})$$

For large numbers ($N \gg 1$, $n \gg 1$, $N-n \gg 1$) this becomes a continuous Gaussian distribution for the net rotation $x = (2n-N)\eta$

$$P(x) = \frac{1}{\sqrt{2\pi}\sigma} \exp\left[-\frac{1}{2} \frac{(x-\bar{x})^2}{\sigma^2}\right], \quad (\text{S.13})$$

with mean $\bar{x} = N(2p-1)\eta$ and standard deviation $\sigma = 2\sqrt{Np(1-p)}\eta$.

The efficiency of the motion can be quantified by the expectation value of $\cos x$ which represents the fraction of the distance covered in the direction of a gradient in x -direction

$$\langle \cos x \rangle = \int_{-\infty}^{\infty} dx \cos x \frac{1}{\sqrt{2\pi}\sigma} \exp\left(-\frac{1}{2} \frac{x^2}{\sigma^2}\right) = \exp\left(-\frac{1}{2}\sigma^2\right). \quad (\text{S.14})$$

In the last equation one can identify the standard deviation σ with the opening angle χ of the force distribution. Thus, this simple model predicts that with increasing χ the efficiency should decrease. As can be seen from Fig. S3 this clearly contradicts our numerical findings. This indicates that the ability to follow the gradient is not determining the efficiency of motion. As we show now, it in fact depends crucially on the ability of the cell to align with the gradient.

To do so, we assume that initially the cell has an angle θ_0 between its major axis and the applied linear gradient. With a probability p the cell now rotates by an angle Ψ towards the gradient. Thus, after $n = \frac{|\theta_0|}{\Psi}$ the cell is perfectly aligned with the gradient.

Here, the efficiency can be quantified by the averaged probability of the cells to align with the gradient

$$\int_{-\pi}^{\pi} d\theta_0 p^{\frac{|\theta_0|}{\Psi}} = 2 \frac{\Psi}{\ln p} \left[\exp\left(\frac{\pi}{\Psi} \ln p\right) - 1 \right]. \quad (\text{S.15})$$

Taking into account that the starting angles θ_0 are Gaussian distributed in our simulations, the efficiency becomes

$$\begin{aligned} \int_{-\pi}^{\pi} d\theta_0 \frac{1}{\sqrt{2\pi}\sigma_\theta} \exp\left(-\frac{1}{2} \frac{\theta_0^2}{\sigma_\theta^2}\right) p^{\frac{|\theta_0|}{\Psi}} &= \frac{2}{\sqrt{2\pi}\sigma_\theta} \int_0^{\pi} d\theta_0 \exp\left(-\frac{1}{2} \frac{\theta_0^2}{\sigma_\theta^2} + \frac{\theta_0}{\Psi} \ln p\right) \\ &= \exp\left[\frac{\sigma_\theta^2 (\ln p)^2}{2 \Psi^2}\right] \left\{ \operatorname{erf}\left[\frac{1}{\sqrt{2}\sigma_\theta} \left(\pi - \frac{\sigma_\theta^2 \ln p}{\Psi}\right)\right] + \operatorname{erf}\left[\frac{\sigma_\theta \ln p}{\sqrt{2} \Psi}\right] \right\}. \end{aligned} \quad (\text{S.16})$$

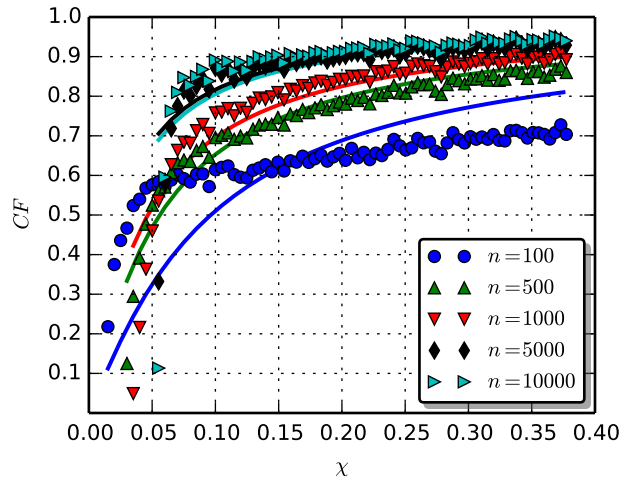


FIG. S3: Efficiency of motion as function of χ and number of time steps n in the simulation. At early simulation stages the efficiency is dominated by the alignment with the gradient. At later times all cells are aligned with the gradient and the efficiency approaches 1. For vertically elongated ellipses ($R_s > 2R_l$) the torque can turn the cell against the gradient resulting in a negative efficiency. If this event occurred the simulation was stopped. The lines show the results of fitting Eq. (S.16) to the numerical data.

Thus, the probability depends on the rotation angle Ψ (that we identify with the opening angle χ of the force distribution) and on the probability p (which depends on the strength of the gradient). Because the exact relation between p and the strength of the gradient is not known we take $\ln p$ as a fitting parameter. As one can see from Fig. S3 the fitted curves match the numerical data quite well for sufficiently large number of simulation steps. At early simulation stages the numerical data depends still on the initial orientation of the cell.

For vertically elongated cell ($R_s > 2R_l$) the gradient eventually turns the cell into the “wrong” direction. This tilt in the wrong direction increases with time since arms growing in this direction are favored by the gradient. This process leads to an alignment of the ellipse against the gradient. We stopped our simulations when such an event occurred.

MODEL FOR BACTERIAL CHEMOTAXIS

To model the bacterial chemotaxis, we use the well-studied swim-tumble model. The cell swims into a random direction for a normally distributed length l . It measures the change in concentration Δc of an attractant along this path. On the basis of Δc the decision is made whether the cell maintains the current direction or tumbles. The former occurs with probability

$$p(\Delta c) = \begin{cases} \frac{p_0}{1 - \frac{\Delta c(1-p_0)^2}{kp_0}} & \Delta c \leq 0 \\ \frac{1}{1 + \frac{k(1-p_0)}{\Delta c + p_0(k - \Delta c)}} & \Delta c > 0 \end{cases} \quad (\text{S.17})$$

which is larger than a basal probability of $p(\Delta c = 0) = p_0$ for $\Delta c > 0$ and smaller than p_0 for $\Delta c < 0$. The parameter k quantifies the stiffness of the response.

To compare this model with our model, we also applied here a concentration gradient with a linear slope in x -direction.

SUPPLEMENTARY FIGURES

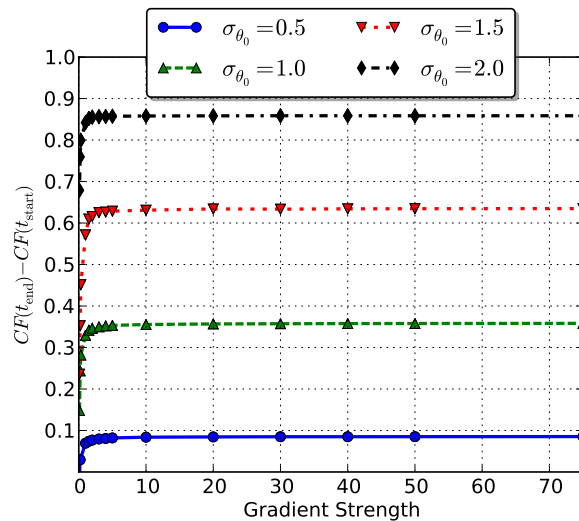


FIG. S4: Gains in chemotactic factor CF , i.e. difference between CF at the end and at the beginning of the simulation, as function of gradient strength c_0 . Results are shown for different standard deviations σ_θ of the initial polarization angle θ_0 . For smaller σ_θ the cells are initially aligned more in the direction of the gradient, so less gain is expected.

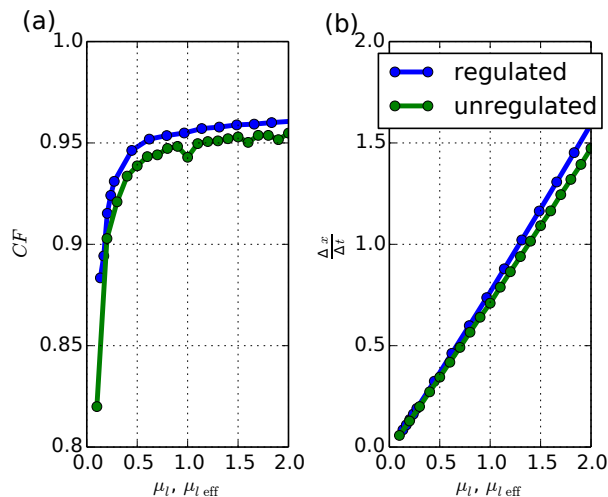


FIG. S5: Effect of the concentration dependent regulation of arm lengths on efficiency of motion. (a) If we increase the average arm length μ_l we see an increase in efficiency that saturates for longer arms. If we use the concentration dependent regulation of arm lengths ($\mu_{l,\text{eff}}$, see Eq. (5)) we get a 1% increase in maximum efficiency compared to the unregulated system from $CF \approx 0.95$ to $CF \approx 0.96$, but the same efficiency is reached with an average arm length up to 40% shorter compared to the unregulated system. (b) Speed of motion, characterized by the covered path length Δx per time unit Δt increases with increasing arm length. Additionally, for identical average arm length motion is faster with regulation. The difference in speed increases with increasing average arm length.

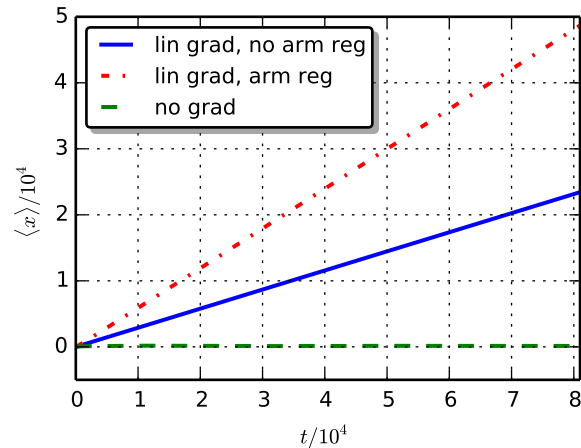


FIG. S6: Classification of the migration dynamics. The cell performs a random walk which is biased in the presence of a gradient, see Fig. 2. If the arms are regulated the motion in absence of a gradient stays the same, whereas the motion in presence of a gradient becomes faster at constant efficiency (additional red dash-dotted line).

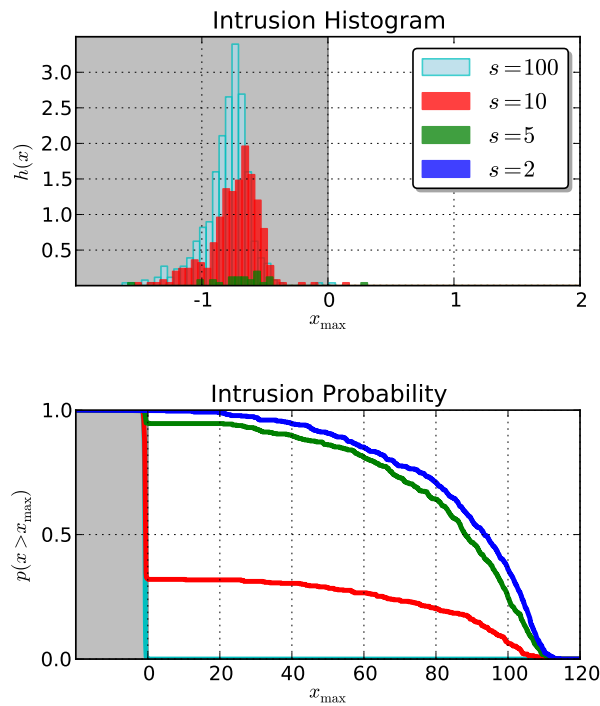


FIG. S7: Histogram and probability of intrusion at a surface step (i.e. interface between stiff and soft substrate region). Cells move from left (grey, stiff substrate) to right (white, soft substrate). The histogram shows the frequency of the maximal (most right) x value reached. We only show the region close to the step to focus on the cells that did not cross it. Cells that have passed the step (most of the cells in simulations for small steps, i.e. blue and green) would be found at $x_{\max} > 2$, so they are not shown in the histogram. For larger step sizes not all cells pass the step. The maximal distance traveled in positive x -direction peaks closer to the interface with decreasing step size. If the step size becomes too small almost all cells pass the step as indicated by the intrusion probability that is defined as the probability that a cell travels further than x_{\max} .

SUPPLEMENTARY TABLES

Parameter	Fig. 2 & S6	Fig. 3	Fig. 4 & S3	Fig. 5	Fig. 6(a)	Fig. 6(b)	Fig. 7	Fig. S2	Fig. S4	Fig. S6	Fig. S7
Iter.	81000	–	–	500	500	500	500	1	500	500	500
Runs	500	500	1000	500	500	500	500	5000000	500	500	500
a	1	1	1	1	1	1	1	1	1	1	1
b	0.5	0.5	–	0.5	0.5	0.5	0.5	0.5	0.5	0.5	0.5
δ	-1	-1	-0.9	–	-1	-1	-1	-0.9	-1	-1	-1
σ_θ	1.047	1.047	1.047	–	–	0	1.047	–	–	1.047	0
k	1	1	1	1	1	1	1	1	1	1	1
c_0	–	1	1	1	1	1	1	–	–	1	1
N	10	–	10	10	10	10	10	1	10	10	10
p_+	0.9	0.9	0.9	0.9	0.9	0.9	0.9	0.9	0.9	0.9	0.9
μ_i	0.5	0.5	0.5	0.5	0.5	0.5	0.5	0.5	0.5	–	0.5
σ_i	0.05	0.05	0.05	0.05	0.05	0.05	0.05	0.05	0.05	0.05	0.05
σ_+	0.5	0.1	0.1	0.5	0.5	0.5	0.5	0.3	0.5	0.5	0.5
σ_-	0.05	0.01	0.01	0.05	0.05	0.05	0.05	0.03	0.05	0.05	0.05
σ_γ	0.7	0.1	0.1	0.1	0.1	0.1	0.1	0.1	0.1	0.1	0.1

TABLE S1: Parameter values for the results shown in Figs. 2-7, S2-S7

Step size s	$\frac{n_{\text{Soft}}}{n_{\text{Stiff}}}$	T_C
2	0.9374	1.0000
5	0.8843	0.9480
10	0.8622	0.3220
100	0.8330	0.0020

TABLE S2: Values for the ratio of refraction indices $\frac{n_{\text{Soft}}}{n_{\text{Stiff}}}$ and transmission coefficient T_C . The refractive effect becomes stronger with increasing step size whereas the transmission decreases.